communications materials

Article

A Nature Portfolio journal

https://doi.org/10.1038/s43246-026-01241-7

Enhanced mid-infrared light-matter coupling in heavily-doped *p*-germanium due to interplay between plasmonic and inter-subband contributions

Check for updates

Aravind N. Subramanian[1,2], Saud Bin Anooz[1], Sergey G. Pavlov[3], Carsten Richter[1], Géza Szántó[4], Mariia Sidorova[5], Peter Petrik[4,6] & R. Radhakrishnan Sumathi[1,2]

The development of germanium-based mid-infrared (MIR) optoelectronic technologies is central to advancing compact, high-performance on-chip systems. While plasmonic field enhancement in heavily-doped semiconductors is widely exploited to intensify light-matter interactions, yet *p*-type germanium has been discarded due to its complex valence band structure. Here, we show that heavily-doped *p*-type germanium exhibits a dual light-matter interaction, where an ε-near-zero band delineates a plasmonic-like regime below the plasma frequency and a broadband absorption (dominated by inter-subband transitions) above it. This duality extends the spectral range of strong interaction beyond conventional Drude plasmonics. Using the Czochralski method, we have grown high-quality heavily-doped germanium single crystals with gallium concentrations up to ~2×10^{20} cm^{-3}, exhibiting a high, near 100% acceptor activation. Mid-infrared spectroscopic ellipsometry and reflectance measurements reveal a continuous blue shift of the plasma wavelength with increasing dopant concentration, up to 4.5 µm, the shortest wavelength reported in Ge to date. Our findings manifest the potential of heavily-doped *p*-type bulk germanium crystals for applications that benefit from strong mid-infrared absorption and high crystal lattice quality.

The development of a scalable on-chip photonic platform is omnipresent in advanced optoelectronic applications[1,2]. A key requirement is compatibility with the widely adopted silicon (Si)-based complementary metal-oxide-semiconductor (CMOS) foundry processes[3]. Among the potential material platforms, germanium (Ge) is particularly attractive due to its small band gap energy (0.66 eV), lower processing temperatures (compared to Si), and high mobility of charge carriers in moderately-doped crystals (for electrons; ≤3900 cm^{2}V^{-1}s^{-1} and for holes; ≤1900 cm^{2}V^{-1}s^{-1})[4].

There has been growing interest in the mid-infrared (MIR) properties of heavily-doped semiconductors, particularly Ge[5–9]. Many molecules exhibit characteristic "fingerprint" absorption bands within the MIR spectrum, enabling precise chemical sensing[10]. A special focus is for materials exhibiting strong light absorption within the MIR atmospheric windows: 3–5 µm and 8–14 µm. Heavily-doped Ge, with its strong MIR absorption, offers a scalable platform for integrated sensors catering to a wide range of applications, including space exploration, environmental pollution monitoring, homeland security and biomedical technology[11,12].

Strong light-matter interaction is fundamental to effective sensing and is commonly realized via plasmonic and free-carrier absorption mechanisms in heavily doped semiconductors. As doping concentrations rise, the plasma frequency, i.e., the characteristic frequency at which the dielectric to metallic-like transition occurs, shifts deeper into the MIR region[6] as described by the Drude equation[13],

$$\omega_p = \sqrt{\frac{\mathrm{nq}^2}{\mathrm{m}^*\varepsilon_0\varepsilon_\mathrm{r}} - \gamma_\mathrm{D}^2} \tag{1}$$

[1]Leibniz-Institut für Kristallzüchtung (IKZ), Berlin, Germany. [2]Ludwig-Maximilians-University (LMU), Munich, Germany. [3]German Aerospace Centre (DLR), Institute of Space Research, Berlin, Germany. [4]Hungarian Research Network, Centre for Energy Research, Institute of Technical Physics and Materials Science, Budapest, Hungary. [5]Humboldt-Universität zu Berlin, Berlin, Germany. [6]Department of Electrical Engineering, University of Debrecen, Debrecen, Hungary.
✉e-mail: radhakrishnan.sumathi@ikz-berlin.de

Here, ω_p is the effective screened/damped plasma frequency, n is the free-carrier concentration, m* is the effective mass of the free-carriers, q is the electron charge, ε_0, ε_r are the permittivity of vacuum and relative material permittivity, respectively. γ_D is the Drude scattering rate given by, $\gamma_D = \tau^{-1} = q/(m^*\mu)$, where μ is the mobility of the free-carriers. Heavily doped semiconductors are considered as favourite candidates for realizing plasmonic structures exhibiting strong light-matter interaction in the MIR spectral region, where noble metals often suffer from low field confinement[5–9]. Achieving these short plasma wavelengths requires ultra-high doping (UHD) concentrations together with a comparatively small effective mass, as implied by (1). In addition to the small effective mass of charge carriers and the ability to reach ultra-high activated dopant densities, Ge exhibits a large refractive index within the MIR spectrum. In *n*-type UHD Ge thin films ($\sim 6 \times 10^{19}\,\text{cm}^{-3}$) markedly stronger MIR light-matter interaction has been demonstrated, driven by enhanced near-field confinement and increased free-carrier absorption[5,6,9]. For UHD crystals, however, preserving lattice quality is essential to limit scattering at crystal defects to retain the high charge carrier mobility, which are key figures of merit for high-speed photodetectors and nonlinear optics.

Among the conventional dopants in Ge, the highest doping concentration $\sim (2 \times 10^{20}\,\text{cm}^{-3})$ achievable via the Czochralski (Cz) growth method is with gallium (Ga). Generally, *p*-type dopants in Ge exhibit higher diffusion rates (except boron), slightly higher equilibrium segregation coefficients and higher equilibrium solubility limits compared to the conventional *n*-type dopants[14]. Leveraging carriers in the light-hole (*lh*) subband of *p*-type Ge ($m^*_{lh} = 0.043m_0$) could offer an additional advantage over *n*-type Ge based platforms where the effective mass of charge carriers is, $m^*_e = 0.12m_0$.

Free-carrier absorption can arise from two principal intra-band processes i.e., direct inter-subband transitions (e.g., between valence-band subbands) and indirect, phonon-assisted intra-band absorption (Drude-like)[15,16]. Inter-band absorption in Ge occurs at comparatively high photon energies and therefore lies predominantly in the near-infrared (and above). By contrast, absorption in the mid- and far-infrared is dominated by intra-band transitions and lattice excitations[17]. In general, direct optical transitions (Fig. 1) are stronger than phonon-assisted (indirect) processes because momentum conservation in the latter requires the simultaneous involvement of a phonon (a photon–carrier–phonon interaction), thereby reducing the transition probability[15,16].

Despite these advantages, *p*-type Ge has been dismissed as unsuitable for plasmonic applications due to the destructive effect of competing inter-subband transitions; this statement was derived from its complex reflectance spectrum, which exhibits "no clear" plasma edge[6]. For holes in the Ge valence band, three subbands with distinct effective masses are typically considered: heavy-holes (*hh*) ($m_{hh}^*= 0.330\ m_0$), *lh* ($m_{lh}^*= 0.043\ m_0$) and split-off subbands (so) ($m_{so}^*= 0.084\ m_0$). In heavily-doped *p*-type Ge, direct inter-valence-subband transitions among these states (*hh*↔*lh* and *hh*↔*so*) occur in the same spectral range as the intra-band Drude response within each subband (*hh*→*hh*, *lh*→*lh*)[17]. This spectral overlap complicates a clean identification of the dielectric-to-metallic transition from reflectance spectra alone, in contrast to *n*-type heavily-doped Ge where the plasma edge more often appears as an abrupt drop in the reflectance at the screened plasma frequency[6].

In this work, we demonstrate the plasmonic response and direct free-carrier absorption of heavily-Ga-doped Ge bulk crystals can be resolved by combining mid-infrared spectroscopic ellipsometry (MIR-SE) with mid-infrared absorption/reflectance (MIR-AR) spectroscopy. Our results reveal that heavily-doped *p*-type Ge exhibits a markedly stronger, and spectrally broader, interaction with MIR light in contrast to UHD *n*-type Ge. This enhancement is driven by pronounced inter-subband absorption, dominated by *hh* to *lh* transitions, which bridges the conventional plasmonic band and the onset of inter-band absorption.

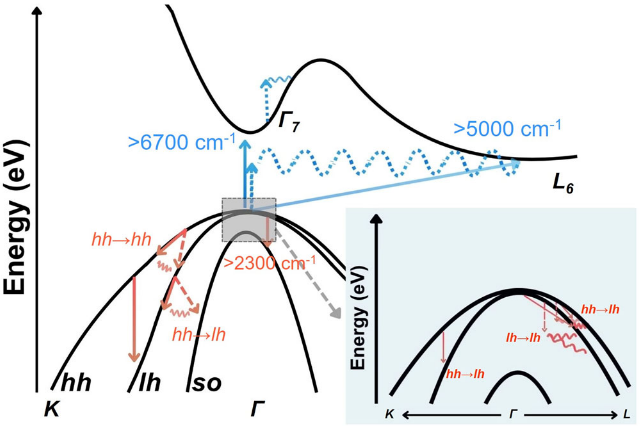

Fig. 1 | Schematic energy band diagram of Ge showing the optical transitions involving free-charge carriers. Vertical arrows indicate direct transitions: NIR inter-band absorption (blue; $\nu \gtrsim 6000\text{cm}^{-1}$, $\lambda \lesssim 1.67\mu\text{m}$) and MIR inter-subband transitions within the valence band (red). Diagonal transitions (and their associated virtual components: photon (vertical line) + phonon (waves) absorption) are indirect transitions of free-charge carriers: NIR inter-band (blue; $\nu \gtrsim 5000\text{cm}^{-1}$),$\lambda \lesssim 2\mu\text{m}$); MIR intra-band (blue, electrons in the conduction band) and intra-subband (red, holes in the valence band).

Results

Crystal structure and dopant incorporation

The Ge:Ga crystal was grown along the <100> crystallographic axis by the Cz method (growth from the melt). The Ge feed material was doped with 10^{21} atoms/cm^3 Ga, such that a high concentration of Ga, exceeding its equilibrium solubility limit in Ge[18] ($> 4 \times 10^{20}\,\text{cm}^{-3}$) is incorporated in the regions towards the end of the crystal.

An X-ray diffraction rocking curve imaging (RCI) map visualizing the crystalline structure of the Ge:Ga crystal is shown in Fig. 2 a. The RCI map confirms that the unit cell volume measured near the top of the crystal, corresponding to a lower Ga concentration (10^{18}–$10^{19}\,\text{cm}^{-3}$) is in good agreement with the standard lattice constant of Ge at 20°C, which is 5.65774 Å[19]. However, it also indicates a slight lattice expansion followed by a distorted crystalline structure due to high Ga concentration ($> 2\times10^{20}\,\text{cm}^{-3}$) towards the lower end of the crystal. Notably, a difference of 0.06 Å^3 was measured between the unit cell volume at the seed end of the crystal (Ga ~ $10^{18}\,\text{cm}^{-3}$) and the poly-crystalline bottom of the crystal (Ga > $10^{20}\,\text{cm}^{-3}$). As the crystalline structure begins to distort, small-angle grain boundaries appear, followed by the formation of cellular structures. The distinct shape of this region and the formation of cellular structures can be explained by the onset of constitutional supercooling at the solid-liquid interface[20]. While doping the Ga melt with high concentrations of Ga, the low equilibrium segregation coefficient of Ga in Ge ($k_0 = 0.087$) leads to excess Ga at the solid-liquid interface. This concentration gradient promotes constitutional supercooling which destabilizes the growth interface and gives rise to characteristic cellular growth morphologies. As a result, the bottom end of the crystal transforms into a poly-crystalline structure with compositional inhomogeneity[21]. Notably, several randomly distributed point-shaped features were observed in the sample cross-section, particularly in the vicinity of the sample edge. Upon further analysis, we attribute these features to the surface irregularities arising from wafer handling. Hall measurements were conducted using the van der Pauw geometry with an applied current of 30 mA at room temperature. The measured distribution of electrically active charge carrier concentration along the crystal length (shown in Fig. 2 b) aligns well with the measured Ga concentration[21], indicating dopant activation close to 100%. Interestingly, an abrupt change in the unit cell volume was observed towards the bottom of the crystal (Fig. 2 a) while maintaining the single-crystalline structure. Hall measurement performed in this region revealed a charge carrier density of ~$2\times10^{20}\,\text{cm}^{-3}$, which is close to the solubility limit of Ga in Ge.

Mid-infrared spectroscopic ellipsometry

The dielectric function (ε) is key to understanding the optical as well as the plasmonic properties of the material. The complex pseudo-dielectric

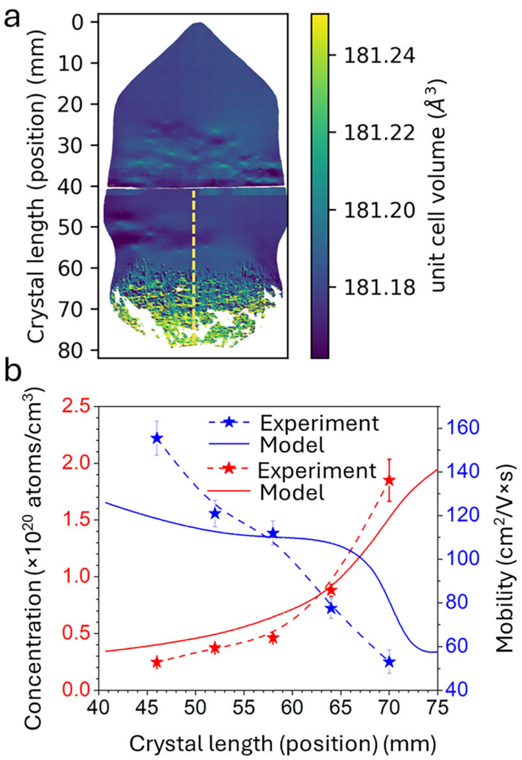

Fig. 2 | Structural evolution and active charge carrier concentration along the Ge:Ga crystal. a Change in the unit cell volume mapped via the RCI method using the asymmetric 333 reflection; dashed line shows the line used to select the points for the ellipsometry; and, **b** The charge carrier concentration and the mobility determined by the Hall measurements performed on probes obtained along the crystal length (marked in yellow in (**a**)) versus the corresponding theoretical values obtained by the Drude-Lorentz model.

function, $\langle\varepsilon(\omega)\rangle=\langle\varepsilon_1(\omega)\rangle + i\langle\varepsilon_2(\omega)\rangle$, characterizes the material's optical response. The real part ($<\varepsilon_1>$) describes the polarizability of the material indicating how it stores and disperses energy from an incident electromagnetic field. The imaginary part ($<\varepsilon_2>$) corresponds to absorption losses, quantifying the energy dissipated into the lattice vibration modes and at free-carrier transitions. The experimentally determined plasma frequency is derived from the zero-crossing frequency of $<\varepsilon_1>$, corresponding to the ε-near-zero band, bridging dielectric-like and metallic-like (plasmonic) bands[22]. The pseudo-dielectric function of the UHD *p*-type region in the crystal was derived from mid-infrared (300–7000 cm^{-1}) spectroscopic ellipsometry. The MIR-SE measurements were performed along the dashed line drawn in Fig. 2 a, corresponding to Ga doping concentration ranging from ~ 3×10^{19} cm^{-3} to ~2×10^{20} cm^{-3}.

The spectral dependences of real $<\varepsilon_1>$ and imaginary $<\varepsilon_2>$ parts of the pseudo-dielectric function of the UHD regions of the crystal in the low-frequency MIR range are shown in Fig. 3 a. In all measured regions of the Ge:Ga crystal, the real part, $<\varepsilon_1>$, exhibits negative values at low frequencies, consistent with a free-carrier–dominated, metal-like (plasmonic) optical response. The plasma frequency, ω_p, is obtained from the zero-crossing of $<\varepsilon_1>$, where $<\varepsilon_1>$ changes sign from positive to negative. Notably, ω_p exhibits a clear blue shift from ~620 cm^{-1} to ~2245 cm^{-1} with increasing free-charge carrier concentration. At the highest doping concentration of ~2×10^{20} cm^{-3}, ω_p rises up to 2245 cm^{-1} (~ 4.45 µm, the shortest wavelength / the highest plasma frequency reported for Ge so far, to our best knowledge). Our results demonstrate that the plasmonic edge in UHD *p*-type Ge is tuneable with an acceptor concentration, analogous to the behaviour observed in UHD *n*-type Ge[5,6,8].

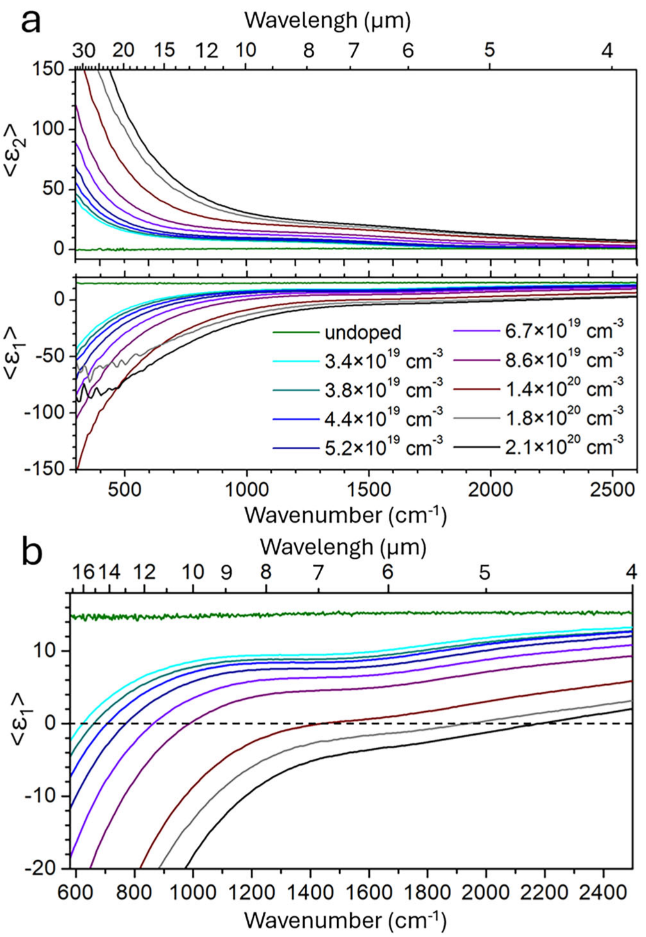

Fig. 3 | MIR pseudo-dielectric response of heavily doped *p*-type Ge. a MIR-SE measurements performed on a sample sectioned parallel to the growth direction of the Ga-doped Ge bulk crystal: real $<\varepsilon_1>$ and imaginary $<\varepsilon_2>$ parts of the pseudo-dielectric function in the low-frequency MIR range, and **b** enlarged region of $<\varepsilon_1>$ around ε-near-zero band.

Mid-infrared absorption spectroscopy

To directly relate the ellipsometry-derived plasma edge to the reflectance response, MIR reflectivity was measured on the same crystal cross-section. Additionally, several Ge samples doped with Ga concentration below the Mott threshold as well as intrinsic/undoped Ge were analysed by transmission and reflection spectroscopies. The transmission measurements of undoped and moderately-doped *p*-type Ge (10^{15} cm^{-3}–10^{16} cm^{-3}) reveal clear spectral features corresponding to both inter-subband (below 400 cm^{-1}) and inter-band transitions (above 5200 cm^{-1}), other spectral features at frequencies below 1000 cm^{-1} are caused by multi-phonon absorption[16] (see Fig. 4 a). In contrast, the UHD Ge (~10^{20} cm $^{-3}$) exhibits negligible transmission across the entire infrared range. Instead, the reflectance spectra of the UHD *p*-type Ge (see Fig. 4 b) provide details on the MIR absorption mechanisms related to free-carrier absorption: intra-subband (with a pole at zero frequency) and inter-subband (with a blue shifted center frequency). In the moderately-doped *p*-type Ge, weak absorption signatures are observed in the low-frequency part of MIR region (primarily due to inter-subband transitions) alongside signatures distinct to inter-band features in the NIR. Inter-subband transitions into the *so* band (≈ 2340 cm^{-1} and above) are comparatively weak and cannot be reliably resolved in the UHD Ge:Ga samples.

In UHD *p*-type Ge, degenerate *p*-type doping shifts the Fermi level into the valence band (Supplementary information; Supplementary Fig. 5). This

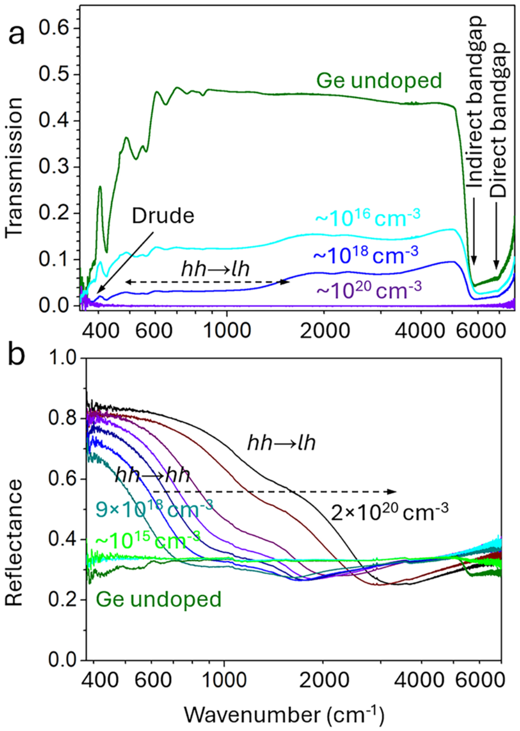

Fig. 4 | MIR-AR spectra of the Ge cross-section marked in Fig. 2 compared to undoped /intrinsic Ge and some moderately-doped Ge samples. **a** transmission spectrum and **b** reflectance spectrum.

increases the population of the free-carriers in the valence band near the Γ-point of the Brillouin zone. This results in an increase of the inter-subband absorption (*hh*→*lh, hh*→*so*) with the dopant concentration (indicated in Fig. 4 b) and a blue shift of the *hh*→*lh* band with increasing doping (Supplementary information; Supplementary Fig. 6). These strong, broadband valence-band transitions mask the plasma edge, therefore ω_p cannot be identified reliably from reflectance alone and instead must be extracted by modelling the reflectivity spectrum. Akin to *n*-type Ge, the high-frequency edge of the reflectance spectrum of the UHD *p*-type Ge cross-section systematically blue shifts with increasing doping concentrations, supporting the tunability of its dielectric function via doping. Notably, at the highest doping levels the inter-subband absorption becomes comparable to the Drude free-carrier response (Supplementary information; Supplementary Fig. 6), effectively filling the spectral interval between the plasmonic band and the onset of inter-band transitions.

The Drude–Lorentz model

To analyze the ellipsometry, reflectance, transmission and absorption spectra of the Ge samples, the complex permittivity (pseudo-dielectric function) was modelled using a dispersion formalism in which the infrared response is determined by oscillator contributions. Following the procedure described in the Supplementary information, the dispersion model was constrained to reproduce only experimentally observed spectral features. The weak lattice absorption below $\sim 700\text{cm}^{-1}$ present in undoped and lightly doped *p*-type Ge was therefore omitted, because it is not resolved in the spectra of UHD *p*-type Ge. Band-to-band (inter-band; bandgap) absorption at $\nu \gtrsim 5300\text{cm}^{-1}$ can, if required, be represented by a constant background term in the high-frequency region (Model (II) in the Supplementary information). Because this contribution lies outside the MIR range of interest, its inclusion does not affect the fit quality in the spectral window used to extract the free-carrier parameters. Other transitions are described using a Drude–Lorentz description of the complex dielectric function, $\varepsilon(\omega)$, similar to the approaches commonly used for UHD *n-type* Ge[6,9],

$$\varepsilon(\omega) = \varepsilon_r - \sum_{\substack{i = hh \to hh,\\ lh \to lh,\\ so \to so}} \frac{S_i {\omega_{pi}}^2}{\omega^2 + i\omega\gamma_i} + \sum_{\substack{j = hh \to lh,\\ hh \to so,\\ lh \to so\\ MPA}} \frac{S_j \gamma_j \omega_{0j}}{(\omega_{0j}^2 - \omega^2) - i\gamma_j \omega} + \varepsilon_{BG}(\omega) \tag{2}$$

where S is the weighting coefficient for each term (proportional to the corresponding oscillator strength), and γ is the damping factor. Furthermore, ε_r denotes the high-frequency (background) relative permittivity, whereas $\varepsilon_{BG}(\omega)$ accounts for additional contributions from optical transitions below and above the band gap, respectively. The first summation (the Drude term, with poles at $\omega = 0$) describes the intra-band response within each subband (*hh*→*hh*, *lh*→*lh* and *so*→*so*). The second summation (Lorentz oscillators, with poles at the resonance frequencies ω_{0j}) captures inter-subband transitions, primarily *hh*→*lh* and (*hh,lh*)→*so*, as well as the contributions of multi-phonon lattice absorption (MPA). Here ${\omega_{pi}}^2 = q^2 n_i / m_i^* \epsilon_0$ are the Drude weights (i.e., the spectral weights of the free-carrier contributions).

The characteristic features preserved in the experimental MIR-SE and MIR-AR spectra indicate two dominant contributions to the mid-infrared response, i.e., intra-band (Drude-like) absorption and inter-subband *hh*→*lh* transitions. Inter-subband transitions into the *so* band (*hh*→*so* and *lh*→*so*) are expected at energies $> 2340\,\text{cm}^{-1}$. Because no detectable features are observed in this spectral range for the UHD Ge:Ga samples, these *so* band related contributions can be neglected within the sensitivity and resolution of the present measurements. The intra-subband *so*→*so* contribution can be neglected because the *so* subband is negligibly populated ($\approx 10^{-6}$ of the total free-hole density). Additionally, separating the intra-band response into two Drude terms (*hh*→*hh and lh*→*lh*) does not improve the fitting of both $<\varepsilon_1>$ and $<\varepsilon_2>$ simultaneously; instead, it drives the fit toward unrealistically high mobilities that are inconsistent with the Hall effect measurements. Furthermore, the real part of the response indicates that ε_r is not constant across the UHD region. Instead of remaining at the commonly accepted value for Ge[6,9], $\varepsilon_r \approx 16$, it varies systematically with both dopant concentration and position within the crystal. We therefore treat ε_r as a fitting parameter. Test fittings indicate that the *hh*→*lh* inter-subband absorption is better captured by multiple Lorentzian-like terms at different resonance energies. The fitting improves substantially when the model is expanded from one to two oscillators, while adding a third yields only marginal further improvement (see Supplementary information for details and the associated model limitations). We therefore limit the number of Lorentz terms in the model, and decompose the real and imaginary parts given by,

$$\mathrm{Re}[\varepsilon(\omega)] = \varepsilon_r(n_i) - \frac{\omega_{hh}^2}{\omega^2 + {\gamma_{hh}}^2} + \sum_{j=hh\to lh} \frac{S_j \Gamma_j \omega_{0j}\left(\omega_{0,j}^2 - \omega^2\right)}{(\omega_{0j}^2 - \omega^2)^2 + \Gamma_j^2 \omega^2} \tag{3}$$

$$\mathrm{Im}[\varepsilon(\omega)] = \frac{\gamma_{hh}\omega_{hh}^2}{\omega(\omega^2 + {\gamma_{hh}}^2)} + \sum_{j=hh\to lh} \frac{S_j \Gamma_j^2 \omega_{0j} \omega}{(\omega_{0j}^2 - \omega^2)^2 + \Gamma_j^2 \omega^2} \tag{4}$$

where $\omega_{hh}^2 = q^2 n_{hh}/(\varepsilon_0 m_{hh}^*)$, $\gamma_{hh} = {\tau_{hh}}^{-1} = q/(m_{hh}^* \mu_{hh})$ is the damping constant related to the *hh* lifetime τ_{hh} and mobility μ_{hh}. The inter-subband term was evaluated using either one or two Lorentz oscillators (Models I and II, respectively). Including a second oscillator yields a slight improvement to the fitting in the spectral range adjacent to the epsilon-near-zero region. The corresponding fit parameters are summarized in the Supplementary information (Tables I and II).

The experimentally observed dependence of the plasma frequency on the free-charge carrier density $\omega_p(n)$, (derived from the zero crossing of $<\varepsilon_1>$ as shown in Fig. 3 b), deviates significantly from the classical Drude model

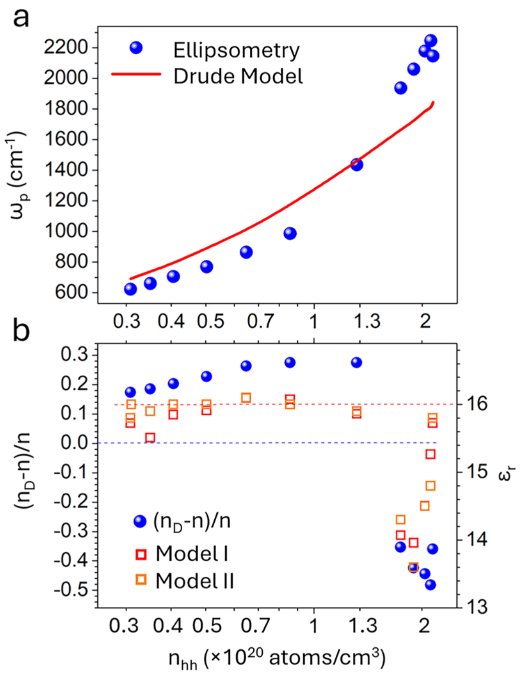

Fig. 5 | Doping concentration dependence of ω_p and the model-derived optical parameters. **a** Experimental values of the plasma frequency as obtained at $<\varepsilon_1> = 0$ from the ellipsometry spectra (blue circles) and the Drude model (Eq. (1)) with the derived (fitted) hh density (assumed to be 0.955 of the total doping) and mobility (assigned to the mobility of hh). **b** Blue circles: Deviation of the free-carrier density from the value n_D, which would be necessary to provide the same plasma frequency; Red and Orange squares: fitted relative permittivity. Note the synchronized, abrupt changes in the slopes at around 10^{20} cm^{-3}, where the lattice transitions to polycrystalline due to ultra-high doping of Ge.

(Eq. (1)), which yields a screened/damped plasma frequency based on the *hh* effective mass and a finite carrier relaxation time (see Fig. 5 a). Notably, two regimes are observed, each characterized by a distinct slope. The abrupt change in slope occurs at approximately the hole density at which crystal growth transitions from a homogeneous single-crystalline region to an inhomogeneous, polycrystalline microstructure (see Fig. 2 a). In this transition region, the extracted lattice parameter shows a slight expansion beyond that of intrinsic Ge, consistent with the presence of tensile strain (or residual tensile stress) in the crystal. Both the fitted high-frequency relative permittivity and the "excess" free-hole density required to support the experimentally observed plasma edge show a pronounced change in trend at this transition.

Below this transition (Ga concentration <10^{20} cm^{-3}), $\omega_p(n)$ follows a Drude-model-like trend, redshifted, with a gradient close to the *hh* mass. The deviation of the measured plasma edge from the value predicted by Eq. (1) can be attributed to a partial depletion of the *hh* population by competing *hh*→*lh* inter-subband absorption. This effect is quantified by taking the Drude limit of Model I (S_j=0, i.e., with the inter-subband oscillators removed) and determining the *hh* density required to reproduce the experimentally observed ω_p as shown in Fig. 5 b.

The evolution of $\omega_p(n)$ above a Ga concentration >10^{20} cm^{-3} cannot be explained by - Eqs. (3) and (4). This may, in part, be explained by: (i) Doping-induced tensile strain can reshape the valence-band dispersion and modify the *hh* effective mass, shifting the expected plasma response. (ii) As the Fermi level moves deeper into the valence band, holes are redistributed among the valence subbands, increasing the *lh* contribution to the plasmonic response and driving ω_p toward a lighter-mass scaling. (iii) The coupling between intra-subband and inter-subband transitions on plasmonic response introducing an additional hybrid pathway that extends the plasmonic-like spectral band toward higher frequencies. The first hypothesis is consistent with the measured change in the lattice constant upon doping, which correlates well with the corresponding changes in the relative permittivity (see Fig. 5 b). By contrast, the hole populations in the valence band of Ge close to the UHD limit are complex phenomenon and would require a dedicated, quantitative treatment of the evolving valence-band dispersion and density of states, as well as doping-dependent intra- and inter-subband scattering rates. A full analysis of these coupled effects is beyond the scope of the present work. Our simplified estimate for redistribution of holes relative to intrinsic Ge, suggests that the screened plasma frequencies measured by MIR-SE in the UHD regime can be reproduced if approximately ~16% of the free holes occupy the *lh* subband. In addition, whether direct inter-subband absorption can itself sustain a plasmonic-like response merits a dedicated analysis beyond the scope of the present work.

In contrast to the simple Drude model, which is limited to intra-subband absorption due to free-carrier oscillations, the Drude-Lorentz model yields a significantly improved fit to the experimental pseudo-dielectric function and the reflectance spectrum; for more details, refer to Supplementary Figs. 3 and S4 given in the Supplementary information. To evaluate the spectral overlap between the plasmonic and inter-subband contributions, a virtual absorption spectrum was constructed (Supplementary information; Supplementary Fig. 6) by selectively suppressing individual Drude/Lorentz terms, thereby isolating the corresponding intra- and inter-subband absorption mechanisms. This decomposition shows that the two mechanisms remain largely spectrally separated. Notably, the absorption coefficient evaluated near the nominal surface-plasmon frequency (taken as $\omega_{sp} = \omega_p/\sqrt{2}$), is dominated by the Drude-type free-carrier response, consistent with the behaviour commonly reported for *n*-type Ge.

Collectively, these findings validate the combined use of MIR absorption/reflection and MIR ellipsometry to reliably characterize free-carrier dynamics and inter-subband contributions in heavily-doped *p*-type Ge. Nevertheless, the accuracy in determining the free-carrier concentrations, contributing to plasmonic phenomena, presents challenges. The crystalline defects associated with high dopant concentration serve as scattering centres for free-carriers, thereby reducing their mobility. This can lead to a deviation of the experimentally measured values (from Hall-effect measurements) from the theoretical models, which typically assume an ideal crystalline lattice.

The complex dielectric function derived in this work provides a quantitative basis for benchmarking the MIR plasmonic performance of UHD *p*-type Ge against other materials considered for the MIR plasmonics, including UHD *n*-type Ge and noble metals, following the approach developed by Dastmalchi et al.[23], and subsequently applied to *n*-type Ge[6,9]. The figures of merit (FOM) extracted for surface-plasmon propagation and field confinement at an air–conductor interface (evaluated at 12 μm, within the long-wavelength atmospheric window) place bulk UHD *p*-type Ge between UHD *n*-type Ge and Au, highlighting a distinct performance niche for this material (Fig. 6). UHD *p*-type Ge typically requires higher activated carrier densities than *n*-type Ge to reach a comparable plasma frequency. On the other hand, UHD *p*-type Ge exhibits higher reflectance on the high-frequency side of the plasma edge, which can increase the contrast used to locate resonance features, an important factor for improving readout sensitivity in plasmonic sensors.

Summary

We have demonstrated that the key MIR optical properties of heavily-doped *p*-type Ge crystals can be adequately analysed by combining infrared reflectance and spectroscopic ellipsometry. Together, these techniques extract both plasmonic-like free-carrier spectral bands and strong inter-subband transitions. Notably, *p*-type Ge exhibits high reflectivity below and above the plasma edge and, additionally, strong absorption above it, a behaviour distinct from *n*-type Ge[5,6,9], where absorption and reflection are moderate near the plasma frequency and transparency re-emerges at higher frequencies. This unique optical response underscores the suitability of UHD *p*-type Ge for applications that benefit from high reflection contrast at the plasma frequency, as well as potential surface and bulk plasmon

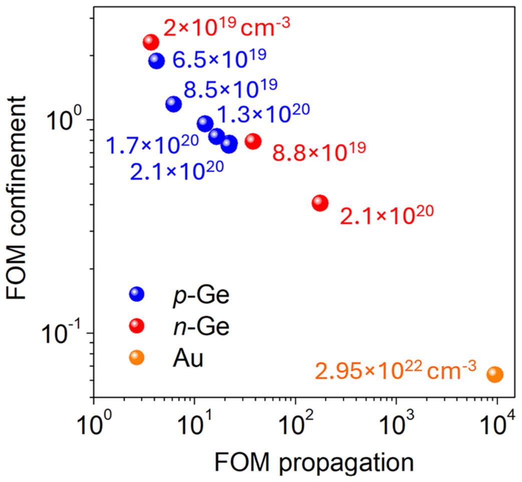

Fig. 6 | Figure of merit for surface plasmon propogation and field confinement. FOM estimated for the p-type Ge samples in this study compared with the estimates for n-type Ge sample No. 9338 (data taken from ref. 9) and gold (data taken from ref. 24). The free carrier concentrations are given. Mid-infrared light wavelength is 12 μm.

excitations. Furthermore, the spectral separation of the maxima of intra-subband and inter-subband absorption preserves the plasmonic properties.

The Czochralski method used to grow HD bulk Ge:Ga crystals yield minimal crystalline defects and eliminates substrate-related interface issues, threading edge dislocations and point defects commonly found in thin films or ion implanted samples, which often produce doped layers with thicknesses less than the light wavelength. The permittivity spectra obtained using MIR-SE reveals a distinct optical transition in regions of the Ge crystal doped with high concentration of Ga (~2×10^{19} to ~2×10^{20} cm^{-3}), from dielectric to a metallic-like optical behaviour. This transition is characterized by the zero-crossing of the real part $<\varepsilon_1>$ of the pseudo-dielectric function, indicating a clear doping-dependent shift in the plasma edge associated with increasing free-carrier density. The plasma-edge frequency is observed to vary from ~620 to ~2300 cm^{-1} (≈16.1–4.4 μm). Notably, achieving the same plasma edge in *p*-type Ge generally requires a higher acceptor density than in *n*-type Ge. Nevertheless, in this work, this has been technically achieved due to the high quality of the bulk crystals and the high activation of introduced Ga. In *p*-type Ge, inter-subband transitions, primarily between *hh* and *lh* states, significantly contribute to the optical absorption, thereby impeding the infrared absorption below the conventional plasma edge (defined solely by the free-carrier oscillations) and increasing reflection above it (defined by strong absorption coefficients at direct MIR transitions). This characteristic extension of strong light-matter interaction in UHD *p*-type Ge beyond the plasmonic band offers a potential alternative to conventional MIR band-gap detector materials based on ternary and quaternary semiconductors.

These results underscore *p*-type Ge as a promising CMOS compatible platform for devices operating in the mid-IR spectral region, in both important MIR atmospheric windows, 3–5 μm and 8−14 μm, crucial for sensing.

Methods

Crystal growth

The crystal growth process was performed using a standard Czochralski puller with a resistance heater made of graphite. To ensure chemical purity of the grown crystal, intrinsically pure Ge feed material (6 N) and 5 N pure metallic Ga granules for doping were used as the starting material. An inert gas atmosphere was maintained during the growth process by continuously flowing argon. The HD Ge:Ga crystal was grown with a constant pulling rate of 30 mm/h. Further information on the crystal growth experiment is given in A. N. Subramanian et al.[21].

X-Ray rocking curve imaging

The measurement was performed on a 0.5 mm thick sample, which was sectioned parallel to the growth axis, such that the (011) oriented wafer exhibits a Ga concentration gradient with the polycrystalline region at the bottom (as indicated in Fig. 2 a). A Rigaku SmartLab X-ray diffractometer was used to perform the RCI measurements. The RCI map was generated by measuring for each of the 333 and $\bar{3}33$ reflections from the (011) oriented cross section wafer involving a rotation about the surface normal by $\varphi = 180°$. The HyPix-3000 2D pixel detector was used to obtain spatial resolution of ~200 μm. A Ge 400 double-crystal analyser was added to obtain angular resolution with regards to the reflected beam. By scanning the sample through the line-shaped X-ray beam with dimensions of 1×8 mm^2 (parallel and perpendicular to the scattering plane), a 4D RCI map comprising the two spatial surface dimensions and, for each point, 2D reciprocal space maps of diffraction intensity near the corresponding 333 Bragg peak were obtained.

Mid-infrared spectroscopic ellipsometry

The MIR-SE measurements were performed using an IR-VASE Mark II ellipsometer supplied by J. A. Woollam. The ellipsometric angles (Ψ, Δ) of the intrinsic Ge and Ge:Ga bulk crystals were measured within the spectral range of 300 cm^{-1}–6000 cm^{-1} at an angle of incidence of 70° at room temperature. To achieve an optimal balance between the spectral resolution and the signal-to-noise ratio, the resolution of the measurements was set to 8 cm^{-1}.

Mid-infrared absorption spectroscopy

A Bruker Fourier Transform Vertex 80 v spectrometer was used for the broad visible to mid-infrared range (0.5–27 μm) bi-directional (13° incidence angle) diffuse reflectance measurements (light spot on a sample between 0.5 and 2 mm, ambient pressure) and transmission (normal incidence angle) measurements. The spectral resolution was set to 1 cm^{-1} or 3 cm^{-1}, depending on the doping.

Data availability

The data that support the findings of this study are available from the corresponding author, upon reasonable request.

Received: 21 October 2025; Accepted: 11 June 2026;

References

1. Hakkel, K. D. et al. Integrated near-infrared spectral sensing. *Nat. Commun.* **13**, 103 (2022).
2. Yang, Z., Albrow-Owen, T., Cai, W. & Hasan, T. Miniaturization of optical spectrometers. *Science* **371**, eabe0722 (2021).
3. Soref, R. Mid-infrared photonics in silicon and germanium. *Nat. Photonics* **4**, 495–497 (2010).
4. Pillarisetty, R. Academic and industry research progress in germanium nanodevices. *Nature* **479**, 324–328 (2011).
5. Prucnal, S. et al. Ultra-doped n-type germanium thin films for sensing in the mid-infrared. *Sci. Rep.* **6**, 27643 (2016).
6. Frigerio, J. et al. Tunability of the dielectric function of heavily doped germanium thin films for mid-infrared plasmonics. *Phys. Rev. B* **94**, 085202 (2016).
7. Fischer, M. P. et al. Plasmonic mid-infrared third harmonic generation in germanium nanoantennas. *Light Sci. Appl.* **7**, 106 (2018).
8. Chong, H. et al. CMOS-compatible antimony-doped germanium epilayers for mid-infrared low-loss high-plasma-frequency plasmonics. *ACS Appl. Mater. Interfaces* **11**, 19647–19653 (2019).
9. Pellegrini, G. et al. Benchmarking the use of heavily doped ge for plasmonics and sensing in the mid-infrared. *ACS Photonics* **5**, 3601–3607 (2018).
10. Schliesser, A., Picqué, N. & Hänsch, T. W. Mid-infrared frequency combs. *Nat. Photonics* **6**, 440–449 (2012).

11. Rieke, G. & Wright, G. A mid-infrared dream come true. *Nat. Astron.* **6**, 891–891 (2022).
12. Butt, M. A., Juchniewicz, M. & Słowikowski, M. Kozłowski, Ł., Piramidowicz, R. Mid-infrared photonic. *Sens. Explor. Fundamentals Adv. Mater. Cut. Edge Appl. Sens.* **25**, 1102 (2025).
13. Sze, S. M., Lee, M. K. Semiconductor Devices: Physics and Technology. (Wiley, 2012).
14. Yonenaga, I., Fornari, R. Germanium crystals. In Single Crystals of Electronic Materials: Growth and Properties 89−127 (Elsevier, 2018).
15. Deinzer, G. & Strauch, D. Two-phonon infrared absorption spectra of germanium and silicon calculated from first principles. *Phys. Rev. B* **69**, 045205 (2004).
16. Ikezawa, M. & Nanba, T. Two-phonon difference absorption spectra in Ge crystals. *J. Phys. Soc. Jpn.* **45**, 148–152 (1978).
17. Kahn, A. H. Theory of the infrared absorption of carriers in germanium and silicon. *Phys. Rev.* **97**, 1647–1652 (1955).
18. Trumbore, F. A. Solid solubilities of impurity elements in germanium and silicon. *Bell Syst. Tech. J.* **39**, 205–233 (1960).
19. Arblaster, J. W. Selected Values of the Crystallographic Properties of the Elements. Selected values of the crystallographic properties of the elements (ASM International, 2018).
20. Tiller, W. A., Jackson, K. A., Rutter, J. W. & Chalmers, B. The redistribution of atoms during the solidification of metals. *Acta Met.* **1**, 428–437 (1953).
21. Subramanian, A. et al. Investigation of doping processes to achieve highly doped Czochralski germanium ingots. *J. Electron. Mater.* **52**, 5178–5188 (2023).
22. Johnson, P. B. & Christy, R. W. Optical constants of the noble metals. *Phys. Rev. B* **6**, 4370–4379 (1972).
23. Dastmalchi, B., Tassin, P., Koschny, T. & Soukoulis, C. M. A new perspective on plasmonics: confinement and propagation length of surface plasmons for different materials and geometries. *Adv. Opt. Mater.* **4**, 177–184 (2016).
24. Olmon, R. L. et al. Optical dielectric function of gold. *Phys. Rev. B* **86**, 235147 (2012).

Acknowledgements

The authors A.N.S., M.S. and R.R.S. acknowledge the partial support from the German Research Foundation (Deutsche Forschungsgemeinschaft) under DFG projects numbers 509105207 and 509113935. Support from the OTKA grant No. K-146181 is gratefully acknowledged. The TKP2021-EGA04 project has been implemented with support from the Ministry of Innovation and Technology of Hungary through the National Research, Development and Innovation Fund. The authors wish to express their sincere gratitude to Dr Nikolay Abrosimov (IKZ) for providing the *n-type* Ge sample and for his valuable support and insightful discussions. The authors thank Dr Andreas Fiedler (IKZ) and Dr Martin Handwerg (IKZ) for their support to perform the Hall effect measurements. The authors acknowledge Dr Hiroki Tanaka (IKZ) for his critical review of the manuscript. The authors would also like to thank Manuela Imming-Friedland, Katrin Berger, and Thomas Wurche from the crystal preparation team at IKZ, Berlin for cutting and polishing the samples. The efforts of Pradeep Chandra Palleti (IKZ) and Alexander Gybin are acknowledged for providing the Ge feed material for crystal growth.

Author contributions

A.N.S.: Conceptualization, Methodology, Data acquisition, Investigation, Formal analysis and Writing—Original draft. S.B.A.: Conceptualization, Data acquisition, Investigation, Formal analysis, Writing—Review and Editing. S.G.P.: Conceptualization, Data acquisition, Validation, Formal analysis, Writing – Review and Original draft, Project administration. C.R.: Data acquisition, Investigation, Formal analysis, Writing—Review and Editing. G.S.: Data acquisition, Formal analysis, Writing—Review and Editing. M.S.: Data acquisition, Investigation, Formal analysis, Modelling, Writing—Review and Editing. P.P.: Data acquisition, Formal analysis, Writing—Review and Editing. R.R.S.: Conceptualization, Methodology, Investigation, Writing—Review and Draft, Supervision, Project administration, Funding acquisition. All authors revised and approved the manuscript.

Funding

Open Access funding enabled and organized by Projekt DEAL.

Competing interests

The authors declare no competing interests.

Additional information

Supplementary information The online version contains supplementary material available at https://doi.org/10.1038/s43246-026-01241-7.

Correspondence and requests for materials should be addressed to R. Radhakrishnan Sumathi.

Peer review information *Communications Materials* thanks Hui Ye and the other anonymous reviewers for their contribution to the peer review of this work. A peer review file is available.